An Atomically Dispersed Mn-Photocatalyst for Generating Hydrogen Peroxide from Seawater *via* the Water Oxidation Reaction (WOR)

Peng Ren[1], Tong Zhang[1], Noopur Jain[2], H. Y. Vincent Ching[1], Aleksander Jaworski[3], Giovanni Barcaro[4], Susanna Monti[5], Joaquin Silvestre-Albero[6], Veronica Celorrio[7], Lata Chouhan[8], Anna Rokicińska[9], Elke Debroye[8], Piotr Kuśtrowski[9], Sabine Van Doorslaer[1], Sandra Van Aert[2], Sara Bals[2], and Shoubhik Das[1]*

[1]Department of Chemistry, University of Antwerp, Antwerp 2020, Belgium.
[2]EMAT and NANOlab Center of Excellence, Department of Physics, University of Antwerp, Antwerp 2020, Belgium.
[3]Department of Materials and Environmental Chemistry, Stockholm University, Stockholm 10691, Sweden.
[4]CNR-IPCF, Institute for Chemical and Physical Processes, Area della Ricerca, Pisa I-56124, Italy.
[5]CNR-ICCOM, Institute of Chemistry of Organometallic Compounds, Area della Ricerca, Pisa I-56124, Italy.
[6]Departamento de Química Inorg´anica, Universidad de Alicante, Alicante E-03080, Spain.
[7]Diamond Light Source Ltd, Harwell Science & Innovation Campus, Didcot, Oxfordshire, OX11 0DE, UK.
[8]Department of Chemistry, KU Leuven, Leuven 3001, Belgium.
[9]Department of Chemical Technology, Jagiellonian University, Krakow 30-387, Poland.

ABSTRACT: In this work, we have fabricated an aryl amino-substituted graphitic carbon nitride (g-C_3N_4) catalyst with atomically dispersed Mn capable of generating hydrogen peroxide (H_2O_2) directly from seawater. This new catalyst exhibited excellent reactivity, obtaining up to 2230 μM of H_2O_2 in 7 h from alkaline water and up to 1800 μM from seawater under identical conditions. More importantly, the catalyst was quickly recovered for subsequent reuse without appreciable loss in performance. Interestingly, unlike the usual two-electron oxygen reduction reaction (ORR) pathway, the generation of H_2O_2 was through a less common two-electron water oxidation reaction (WOR) process in which both the direct and indirect WOR processes occurred, namely photoinduced h^+ directly oxidized H_2O to H_2O_2 *via* a one-step $2e^-$ WOR and photoinduced h^+ first oxidized a hydroxide (OH^-) ion to generate a hydroxy radical (•OH), and H_2O_2 was formed indirectly by the combination of two •OH. We have characterized the material, at the catalytic sites, at the atomic level using electron paramagnetic resonance (EPR), X-ray absorption near edge structure (XANES), extended X-ray absorption fine structure (EXAFS), high-resolution transmission electron microscopy (HR-TEM), X-ray photoelectron spectroscopy (XPS), magic-angle spinning (MAS) solid-state nuclear magnetic resonance (NMR) spectroscopy and multi-scale molecular modeling, combining classical reactive molecular dynamics (RMD) simulations and quantum chemistry (QC) calculations.

INTRODUCTION

The development of single-atom catalysts (SACs) by dispersing metals onto selected supports, such as zeolites, MOFs, COFs, carbon carriers, oxides and carbon-nitride, has seen a recent surge in designing efficient heterogeneous catalysts[1-6]. This strategy undoubtedly enhances the use of isolated dispersed metal atoms, providing more active sites compared to the corresponding metal clusters and nanoparticle forms[7,8]. Practically, it has been proven that, relative to the use of the basic support materials, SACs can enhance the catalytic reactivity and selectivity in specific reactions[9-13]. Furthermore, exploiting the advances in X-ray absorption near edge structure (XANES)[14,15], extended X-ray absorption fine structure (EXAFS) and solid-state nuclear magnetic resonance (NMR)[16-19], a complete picture of the heterogeneous catalytic processes can be provided in some cases[3,20]. While metals such as Fe, Ni, Ru, and Pt have been extensively investigated as SACs, other 3d transition metals (from Sc to Mn), have been less explored due to their lower reactivity, even though they are less toxic and expensive[21-24].

Applying the above methodology for the production of H_2O_2 can be a very efficient strategy that complies with several environmentally responsible requirements. This is because H_2O_2 has been widely used as a highly efficient green oxidant in organic industrial synthesis, in pulp and paper bleaching industries, in sewage treatment, and as a disinfectant[25,26]. It has been directly utilized to generate electricity in one-compartment fuel cell[27,28] because it has an energy density comparable to that of H_2 (60 wt% H_2O_2 has an energy density of 3.0 mega joules (MJ) l^{-1}, higher than compressed H_2 gas at 35 MPa, 2.8 MJ l^{-1}) but has more accessible storage and transportation possibilities. Therefore, the annual global market share of H_2O_2 is expected to grow to 5.7 million tons by 2027, creating overwhelming interest in the sustainable generation of H_2O_2.

The artificial synthesis of H_2O_2 *via* photocatalytic oxidative transformation of water has become a highly promising alternative[1,29-31]. Tremendous efforts have been made by using different homogeneous photocatalysts[27], clusters, nanoparticles[32-38] and SAC-based materials, where

Sb[39] and Pd[40] were atomically dispersed on carbon nitrides and exfoliated graphitic carbon nitrides, respectively. Furthermore, SACs based on Ni/Cu (where Ni and Cu were incorporated into polymeric carbon nitride skeleton[41]) and Ir/Pd (where Ir or Pd atoms were anchored on the MOF nodes[32]) were also successfully developed for the photocatalytic generation of H_2O_2. All these SAC-based photocatalysts followed the two-electron oxygen reduction reaction (ORR) pathway (**Scheme 1**: **equations 1, 2 and 5**), where the formation of intermediate μ-peroxide occurred at the single atomic sites. In most cases, the presence of sacrificial proton donors, such as ethanol, 2-propanol, and benzyl alcohol, was essential to accelerating the separation of the electron-hole pair for a reactivity improvement. In contrast, water oxidation reaction (WOR) by SACs, where photoinduced holes (h^+) (1) directly oxidize H_2O to H_2O_2 *via* a one-step $2e^-$ WOR (**equation 6**) and/or (2) oxidize H_2O to generate hydroxyl radicals ($^{\bullet}OH$) that are able to recombine to produce H_2O_2 (**equations 7-9**)[30,42-44], has been rarely investigated. It is worth mentioning that 97% of the entire water on earth is seawater, and only 3% is fresh water. The presence of various salts in seawater often leads to the deactivation of the photocatalysts, thus limiting their practical application[45,46]. While some signs of progress have been achieved in electrocatalysis, the photocatalytic approach is still in its infancy[45,47-56], and still no report exists on SAC-based photocatalysts using seawater to produce H_2O_2.

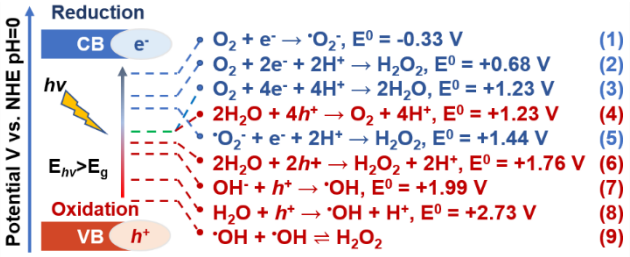

Scheme 1. Energy diagram for the photocatalytic O_2 reduction and H_2O oxidation to H_2O_2, showing the relevant standard potentials.

Considering all these factors, we focused on developing an Mn-based SA PhotoCatalyst (SAPC) to generate H_2O_2 directly from seawater under the irradiation of visible light. The rationale was that the utilization of Mn is highly advantageous due to the inherent tailoring of the charge transfer dynamics by Mn[57-59]. In fact, Mn^{2+} ions prolong the photoluminescence lifetime, which is ideal for the seawater treatment since the level of salts hastens the electron-hole charge recombination process, destroying the photocatalyst. Expediently, Mn has low crystal-field activation energies for the change of the oxidation state during the WOR compared to the second- or third-row transition metal ions and plays significant roles in enzymatic processes[60]. We also argue that the modified graphitic carbon nitrides should act as a superior host for this SAPC material where the abundance of active imine sites (C=N) should facilitate the catalytic reactivity[7,61,62]. Moreover, recent studies have also revealed that the presence of Mn in these systems can increase corrosion resistance from seawater[63]. Interestingly, a less common two-electron WOR process obtained a full catalytic performance of the proposed Mn-based SAPC. Additionally, we found that the oxidation state of Mn was +2 with two distinct types of environments in the catalyst structure: the six-coordinated moiety and the "edge" environment functionalized with an aryl amino group. Using SAPC to enhance both the reduction and oxidation reactions provides a framework for creating more sophisticated photocatalytic systems with broad applications.

RESULTS AND DISCUSSION

Photocatalytic H_2O_2 production on Mn-SAPCs: Atomically dispersed Mn on aryl amino substituted g-C_3N_4 was obtained by a consecutive impregnation-calcination process (the detailed procedure is reported in the Supporting Information). Initially, dicyandiamide (DCDA) and the co-material, 2-aminobenzonitrile were reacted with $Mn(NO_3)_2{\cdot}4H_2O$. Afterward, the reaction mixture was pyrolyzed at 550 °C under air to give Mn/AB-C_3N_4. To compare the reactivity of Mn/AB-C_3N_4 with other structures, Mn-free AB-C_3N_4 was also synthesized by mixing DCDA and 2-aminobenzonitrile. And the Mn-doped g-C_3N_4 catalyst (Mn/g-C_3N_4) was synthesized by mixing DCDA (as the precursor for graphitic carbon nitride) and $Mn(NO_3)_2{\cdot}4H_2O$.

After the synthesis of these SAPCs, we assessed the photocatalytic performance of Mn-SAPCs for H_2O_2 production. In a typical procedure, 0.04 g of Mn/AB-C_3N_4 catalyst was dispersed in 22 mL of oxygen-saturated deionized water under continuous stirring. After dark adsorption for 10 min, the mixture was illuminated with a Kessil LED lamp (λ = 427 nm) under ~8000 lux photon flux density (light intensity 196 mW/cm^2), and the reaction temperature was maintained at 10°C using a cooling water bath system. The suspension was sampled, filtered, and analyzed at regular intervals. The concentration of H_2O_2 was determined by using the redox $KMnO_4$ titration method (Supporting Information **S1.4**).

When acid was used as a sacrificial proton donor or under neutral conditions, either under dioxygen or under air, only a negligible amount of H_2O_2 was detected (**Figure 1a**). In contrast, the reaction provided a higher yield in an alkaline medium (0.55 M NaOH) under both dioxygen and air (**Figure 1a**). Given these indications, after testing other metal hydroxide additives such as LiOH, NaOH, KOH and CsOH (**Figure 1b**), we found that the optimized conditions were achieved when the reaction was carried out using a 0.55 M KOH solution in both dioxygen and air. Among them, a reasonable H_2O_2 concentration of 3250 μM (**Figure 1b**) was obtained in dioxygen by using KOH after 7 h, which is ca. 4.7 times higher than using NaOH (690 μM) and 7.6 times higher than using LiOH (430 μM). Considering the dissociation abilities of these alkali metal hydroxides in water (LiOH: pK_b = 0.18, NaOH: pK_b = -0.56, KOH: pK_b = -1.1, and CsOH: pK_b = -1.76), we can deduce that the higher the degree of dissociation, the more the base can promote the reaction. However, the generation of H_2O_2 from CsOH was lower than KOH, although the higher pK_b value of the former indicated a possible involvement of the cation in the process of H_2O_2 generation. To disclose the influence of the pH on the Mn/AB-C_3N_4-catalysed H_2O_2 photoproduction reaction, different concentrations of KOH (0.045 M, 0.14 M, 0.27 M, and 0.55 M, and 0.82 M) were individually tested in

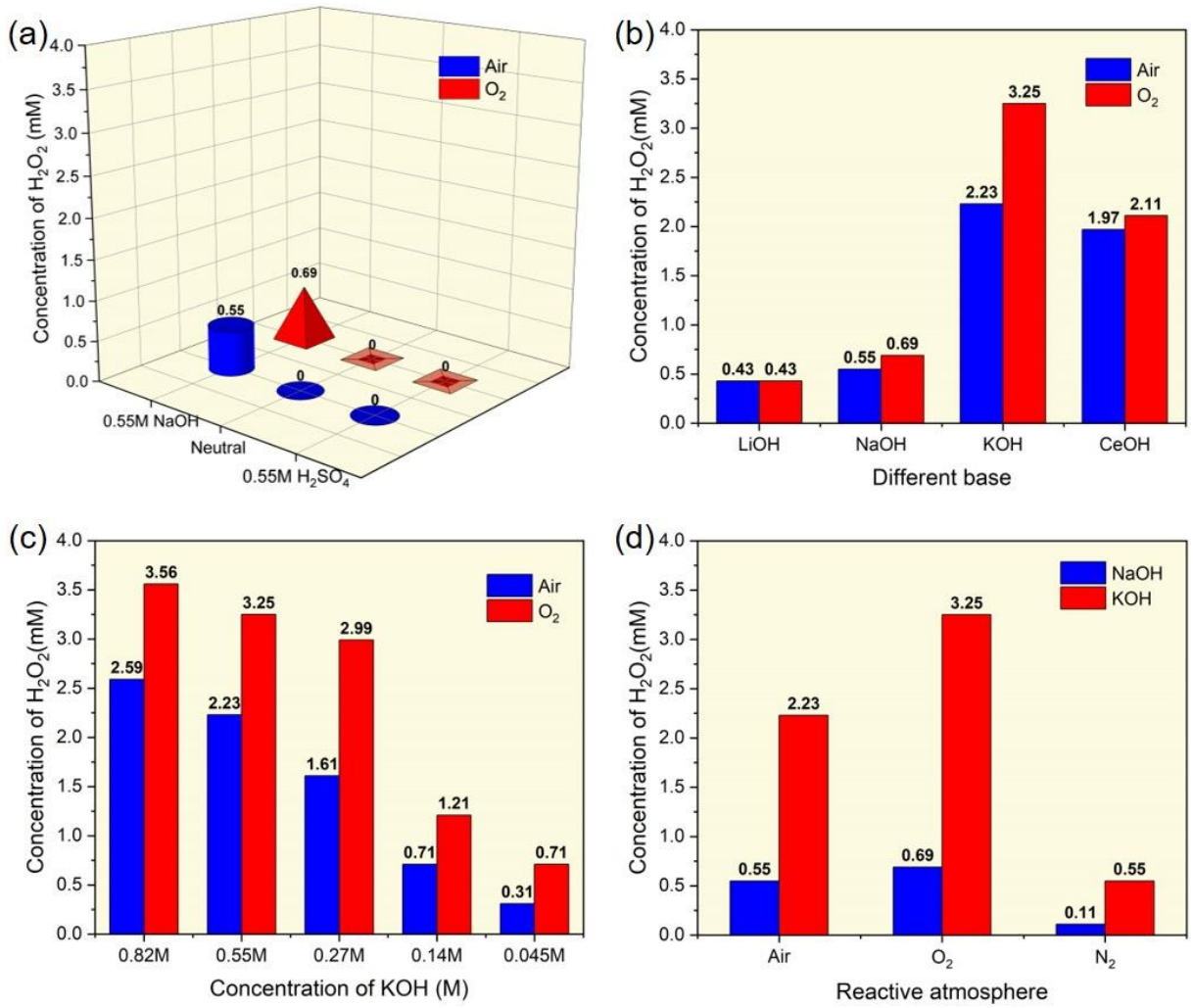

Figure 1. (a) Photocatalytic H_2O_2 production using the Mn/AB-C_3N_4 catalyst under different pH medium. Conditions: Mn/AB-C_3N_4 photocatalyst (1.8 g/L),) and base or acid (0.55 M) in deionized water (22 mL); (b) Photocatalytic H_2O_2 production using Mn/AB-C_3N_4 catalyst with various alkali metal hydroxide. Conditions: Mn/AB-C_3N_4 photocatalyst (1.8 g/L) and alkali metal hydroxide (0.55 M) in deionized water (22 mL). (c) Photocatalytic H_2O_2 production using the Mn/AB-C_3N_4 catalyst with different concentrations of KOH. Conditions: Mn/AB-C_3N_4 photocatalyst (1.8 g/L) in deionised water (22 mL); (d) Photocatalytic H_2O_2 production using the Mn/AB-C_3N_4 catalyst under different reaction atmospheres. Conditions: Mn/AB-C_3N_4 photocatalyst (1.8 g/L) and KOH (0.55 M) in deionized water (22 mL). Triplicates with <1% error.

deionized water: a steady increase in H_2O_2 production for values of KOH concentration up to 0.27 M was observed (**Figure 1c**). Regarding the dependance on atmospheric conditions of photocatalytic H_2O_2 production in deionized water using the Mn/AB-C_3N_4, no significant difference was observed between oxygen and open-air systems, although the content of H_2O_2 obtained by the reaction under oxygen was higher. This suggested an efficient adsorption−desorption process of the O_2 molecules on the surface of the Mn/AB-C_3N_4 catalyst and that oxygen reduction might not be the rate-determining step, as the catalyst generated almost the same amount of H_2O_2 under air and oxygen atmosphere. Control experiments revealed that Mn/AB-C_3N_4 exhibited a significantly lower reactivity under a nitrogen atmosphere, strongly indicating that O_2 is essential in this reaction system (**Figure 1d**). No reactivity was observed without the catalyst or light under identical conditions, which meant that catalyst and light were both essential.

Considering different catalyst compositions, it was found that the Mn/AB-C_3N_4 variant yielded the highest amount of H_2O_2 in the presence of 0.55 M KOH (**Figure 2b**). Notably, we further investigated the H_2O_2 production efficiency in seawater to demonstrate the potential of large-scale application. Although the high concentrations of ions and organic components present in seawater tend to severely hamper the photocatalytic performance of the photocatalyst by impeding their intrinsic structure and electron transport capabilities[49], in our standalone reaction in seawater collected from the North Sea, a H_2O_2 concentration of 2250 μM was obtained after seven hours under an O_2 atmosphere (**Figure 2c**). Moreover, the time-dependent H_2O_2 formation experiments were performed in both deionized water and seawater using the Mn/AB-C_3N_4, and from there, it was clear that the yield of H_2O_2 almost linearly increased for the first seven hours (**Figure 2d**). Most importantly, the H_2O_2 concentration continued to grow even after 48 h in pure water and seawater, which

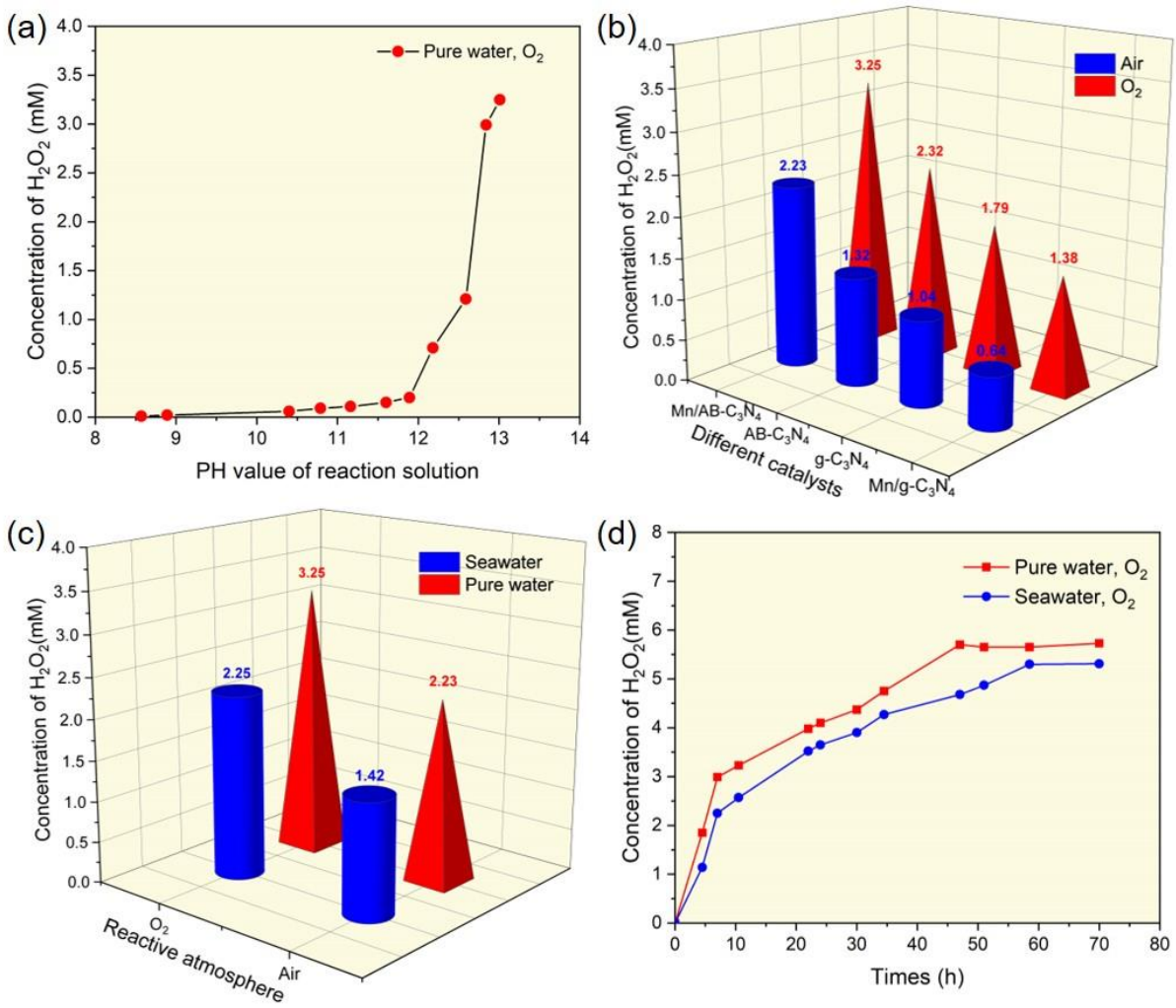

Figure 2. (a) Photocatalytic H_2O_2 production using the Mn/AB-C_3N_4 catalyst under different pH. Conditions: 1.8 g/L Mn/AB-C_3N_4 catalyst in deionized water (22 mL) under O_2; (b) Photocatalytic H_2O_2 production using other modified g-C_3N_4 catalysts. Conditions: 1.8 g/L catalyst and 0.55 M KOH in deionized water (22 mL). (c) Comparison between deionized water and seawater under different reaction atmospheres. (d) Kinetic experiment of photocatalytic H_2O_2 production in deionized water and seawater. Sampling (1 mL) was done at every time using the Mn/AB-C_3N_4 catalyst. Triplicates with <1% error.

showed the high durability of the Mn/AB-C_3N_4 photocatalyst (**Figure 2d**). This result suggested that this catalyst had very high stability in salty environments, which should bring enormous potential for seawater utilization for the sustainable generation of H_2O_2. We subsequently investigated the recyclability of the catalyst Mn/AB-C_3N_4 under optimized conditions. In fact, the catalyst was used 5 times consecutively with minor variations in reactivity in pure water and seawater, indicating the high stability of Mn/AB-C_3N_4 (**Figure S3**).

Characterization of Mn-SAPCs. We carefully investigated the structural characteristics of the as-synthesized catalysts to understand the excellent photocatalytic performance of Mn-SAPCs for H_2O_2 production using various techniques. First, Mn/AB-C_3N_4 was characterized by low-magnification energy-dispersive X-ray spectroscopy (STEM-EDS) mapping before its application in the reaction. The EDS elemental maps shown in **Figure 3** confirmed that Mn was uniformly dispersed over the C_3N_4 support (see supporting Information, **Figure S4**). We quantified the Mn loading from various regions over the sample, and we found 0.07-1 atom%. Finally, to confirm the successful formation of single atomic metallic sites, we used high-resolution high-angle annular dark-field transmission electron microscope (HAADF-STEM) imaging to distinguish the heavier metallic element (Mn) over the support. The high-resolution HAADF-STEM image in **Figure 3b** shows high contrast for specific sites, indicating Mn atomic sites possibly randomly distributed on the C_3N_4 support. Some of the sites are highlighted with red circles to guide the reader's eye to such high contrast features. It is to be noted that along with single-atomic sites, the presence of Mn clusters is also possible. It is difficult to distinguish clusters from single-atom sites in some specific areas of the substrate due to difference in thickness and overlapping of contrast from the same. Similar results were also obtained for the catalysts after the photocatalytic reaction (**Figure 3c-d**), confirming their stability once again.

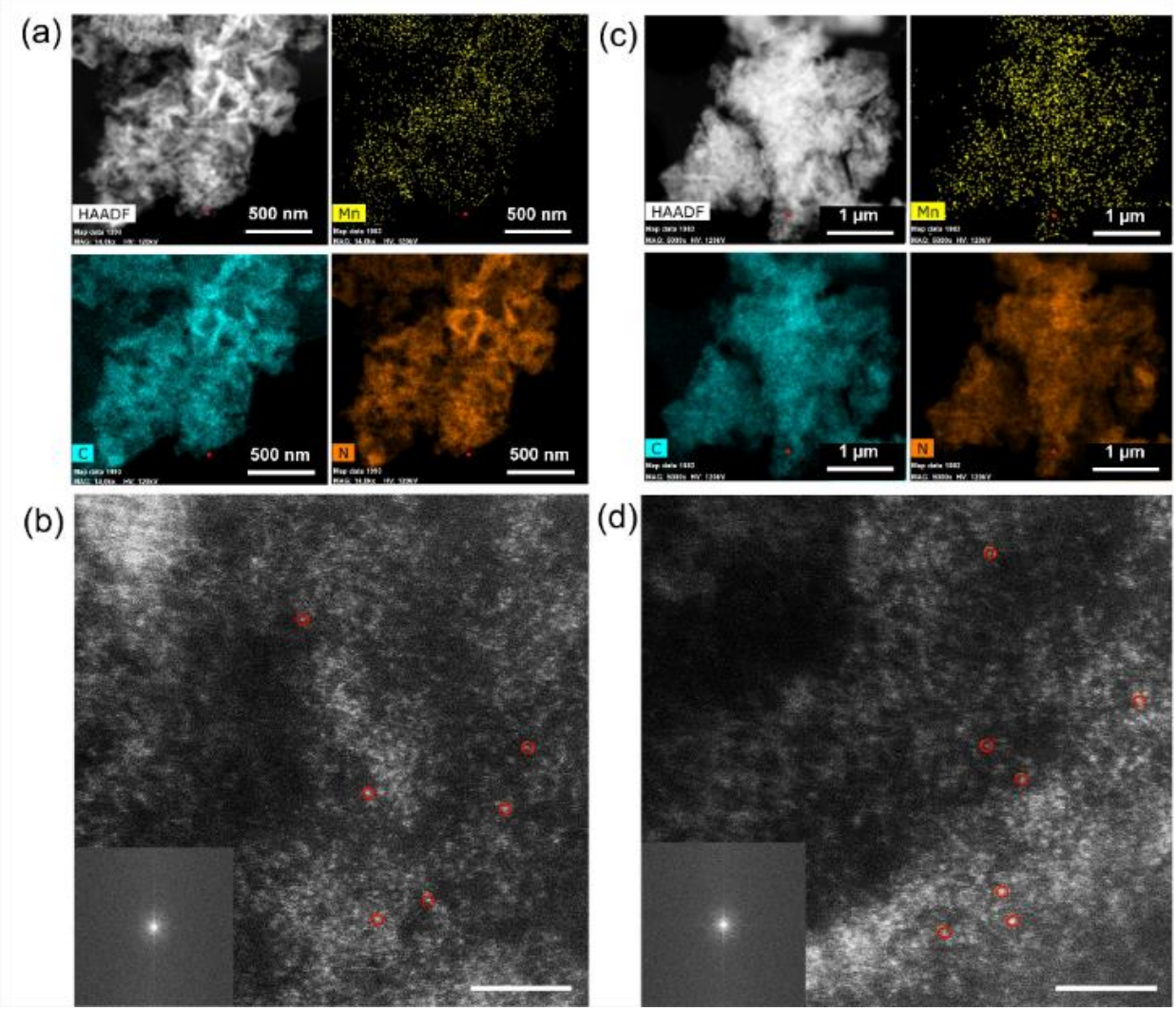

Figure 3. Before reaction: (a) Low-magnification STEM-EDS elemental maps showing the presence of Mn, C, and N on the catalyst (scale bar: 500 nm). (b) HAADF-STEM image of atomic-scale Mn sites dispersed on C_3N_4 support (before reaction) and FFT in the inset showing an absence of periodicity in the dispersion of atoms (scale bar: 2 nm). After reaction: (c) Low-magnification STEM-EDS elemental maps showing the presence of Mn, C, and N on the catalyst (scale bar: 1µm) and d) HAADF-STEM image showing atomic-scale sites on Mn dispersed on C_3N_4 (after reaction, scale bar: 2 nm).

XPS analysis provided further insight into the surface composition of Mn/AB-C_3N_4 (**Figure S6**). Before the photoreaction, the main component of the surface of the photocatalyst was the g-C_3N_4 phase. Its presence was manifested in both the N 1s and C 1s regions. For the C 1s region, a dominant peak at 288.1 eV, assigned to sp^2-bonded carbon (N–C=N), was observed. Adventitious carbon species present on the surface provided only a trace peak at 284.8 eV. In turn, in the N 1s region, photoemission corresponding to nitrogen atoms in three different environments – sp^2-hybridized N in C–N=C (398.6 eV), bridging N atoms N-$(C)_3$ (400.1 eV) and N in amino groups (401.2 eV) - was registered[64,65]. It is worth noting that the composition of the surface practically did not change after the reaction. Additionally, the lack of visible features in the Mn 2p XPS spectrum indicated a very high degree of metal dispersion, which was not disturbed during the process. These results confirm the high reusability of the Mn/AB-C_3N_4 catalyst.

To probe the local structure and examine potential structural changes in the AB-C_3N_4 upon doping with manganese ions, magic-angle spinning (MAS) NMR spectra from all NMR-active nuclei in the material (^1H, ^{13}C, and ^{15}N) were collected. The corresponding ^1H MAS, ^{13}C, and ^{15}N cross-polarization (CPMAS) NMR spectra of the AB-C_3N_4 sample as well as its Mn-doped counterpart (Mn/AB-C_3N_4) are shown in **Figure 4a-c.** The ^{13}C and ^{15}N spectra of samples AB-C_3N_4 and Mn/AB-C_3N_4 are identical. Hence, we concluded that the presence of dopant ions did not significantly alter the material's structure. However, we observed a decrease in ^1H signal intensity for the Mn/AB-C_3N_4 sample compared to AB-C_3N_4. This effect can be attributed to paramagnetic relaxation enhancement for ^1H nuclei in close contact with the Mn^{2+} ions, or partial deprotonation of the >NH and -NH_2 moieties upon Mn doping. The extent of this effect was slightly greater for the -NH_2 groups (relatively more pronounced ^1H signal loss). In general, the respective spectra of AB-C_3N_4 and Mn/AB-C_3N_4 materials closely resemble NMR data collected from the

related polymeric carbon nitride catalysts reported by some of us recently[66,67]. Therefore, we could conclude that the overall structure and polymerization of these materials are very similar. **Figure 4d-e** show the room temperature W-band (~95 GHz) and X-band (~9.5 GHz) continuous-wave (cw) EPR spectra of Mn/AB-C_3N_4, respectively. The X- and W-band EPR spectrum was simulated using three components: Mn', Mn", and gCN (**Table S2**). In the W-band EPR spectrum, Mn', is a typical 6-line powder spectrum arising from the central -1/2→+1/2 transitions of an isolated mono-nuclear high-spin (S=5/2) Mn^{2+} center; its ^{55}Mn (S=5/2) hyperfine coupling (^{55}Mn A_{iso}) is 258 MHz, which is consistent with an Mn^{2+} center coordinated to nitrogen donor ligands[68-70]. Mn" is a second isolated mono-nuclear high-spin Mn^{2+} center with ^{55}Mn A_{iso} = 240 MHz (also consistent with nitrogen ligation), while gCN is a S=1/2 EPR signal arising from the graphitic carbon nitride[71]. The difference in line widths of the Mn' and Mn" signals was simulated by giving Mn' smaller zero-field splitting (ZFS) parameters (D and E) than Mn". The spectral influences of the ZFS interaction are more pronounced at lower microwave frequencies and can be seen in the full X-band spectrum (see **Figure 4e**, comparison between simulated spectra in green and blue). Both X- and W-band EPR spectra were successfully simulated using identical EPR parameters for the three components. There was no need to assume the presence of dimers or multimers with exchange coupling and/or strong dipolar coupling between the Mn(II) sites. Small dipolar interactions due to neighboring Mn(II) sites with an inter-nuclear distance larger than 2 nm will not be visible in cw EPR and may thus occur.

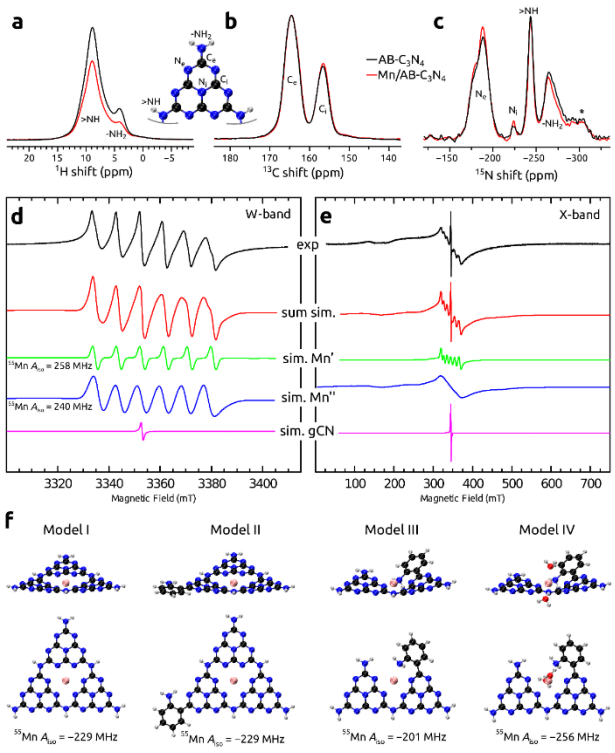

Figure 4. (a) ^{1}H MAS, (b) ^{13}C CPMAS, and (c) ^{15}N CPMAS NMR spectra of the AB-C_3N_4 catalyst and the Mn/AB-C_3N_4 catalyst. (d) cw W-band and (e) cw X-band EPR spectra of Mn/AB-C_3N_4 catalyst and the respective EPR signals deconvolution. (f) models of the environments of the paramagnetic Mn^{2+} ions in the catalyst and the calculated ^{55}Mn hyperfine coupling constants.

To provide further interpretation of the Mn' and Mn" components (**Figure 4d-e**), we created simplified models of possible environments surrounding the Mn^{2+} ions in the Mn/AB-C_3N_4 catalyst and energy-optimized them at the DFT level (with the PBE0-D4 xc-functional, Grimme D4 correction, and the def2-TZVP basis set for Mn and def2-SVP for H,C,N,O, see **Figure 4f**. The ^{55}Mn A_{iso} was subsequently calculated for each model at the coupled cluster level of theory with the DLPNO-CCSD approach[72,73] and the aug-cc-pVTZ-J basis set for Mn and EPR-II for H,C,N,O (**Table S3**). With the predicted ^{55}Mn A_{iso} values, we could correlate the Mn' and Mn" components to two distinct types of environments around the Mn^{2+} ions present in the catalyst structure: the six-coordinated moiety represented by Models I/II with calculated ^{55}Mn A_{iso} = −229 MHz, and the "edge" environment characterized by Model IV with calculated ^{55}Mn A_{iso} = −258 MHz. The sign of the coupling constant cannot be determined from the experimental data. These models were extended (**Figure 7a**) to estimate distances between the two Mn^{2+} cations and the neighbouring N atoms at the edges of the triazine rings and possible reaction mechanisms.

The presence of isolated Mn single atoms active sites was confirmed further by analyzing the Mn/AB-C_3N_4 sample through X-ray adsorption near-edge structure (XANES) and extended x-ray absorption fine structure (EXAFS) experiments at the Mn K-edge, which are a clear fingerprint of the valence state and neighbouring environment of the Mn atoms in the support matrix, respectively. **Figure 5a** compares the Mn K-edge XANES spectra of the photocatalyst with the reference spectra of MnO, Mn_2O_3, and MnO_2, showing that Mn/AB-C_3N_4 is mainly constituted of Mn (II) sites. **Figure 5b** shows the Fourier transform (FT) of the EXAFS data for the Mn/AB-C_3N_4 system, in comparison with the different Mn references. FT shows a single peak at 1.72 Å (without phase correction) corresponding to the first coordination shell, Mn-O/Mn-N[74-76]. The absence of a second peak at a greater distance (R) constitutes further evidence of the isolated nature of the Mn^{2+} sites (M-SACs). These findings are in perfect agreement with HAADF-STEM results described above. **Figure 5c-d** show the comparison between the Fourier transform (FT) of the experimental spectra (empty circles) and the best-fit simulations (colored lines) for the synthesized material. The starting model to fit the data was constructed using the model obtained in **Figure 4f**. The coordination numbers, bond lengths, Debye-Waller factors (σ^2) and the energy shift parameter (ΔE_0) were refined. The best-fit parameters are summarized in **Table S4**. The first shell best-fit results show that each Mn atom is coordinated with 4.6 N/O atoms on average and can be fitted well with the optimized DFT model and RMD simulation results.

Photovoltaic properties of Mn-SAPCs and photocatalytic mechanism: The optical properties and the band diagram of Mn-SAPCs were also investigated. In the beginning, the electronic band structures were determined by UV–vis DRS spectroscopy combined with Mott-Schottky

measurements. The UV-DRS Tauc plot revealed that all four photocatalysts exhibited adequate bandgap in the visible light region (**Figure 6a**): g-C_3N_4 2.68 eV, Mn/g-C_3N_4 2.61 eV, AB-C_3N_4 2.56 eV, and Mn/AB-C_3N_4 2.60 eV. Therefore, it was confirmed that the insertion of aryl amino groups lowers the material band gap, enhancing the absorption of visible light from the environment[66]. Mott-Schottky measurements showed the flat-band potentials positions (E_{fb}) of the g-C_3N_4

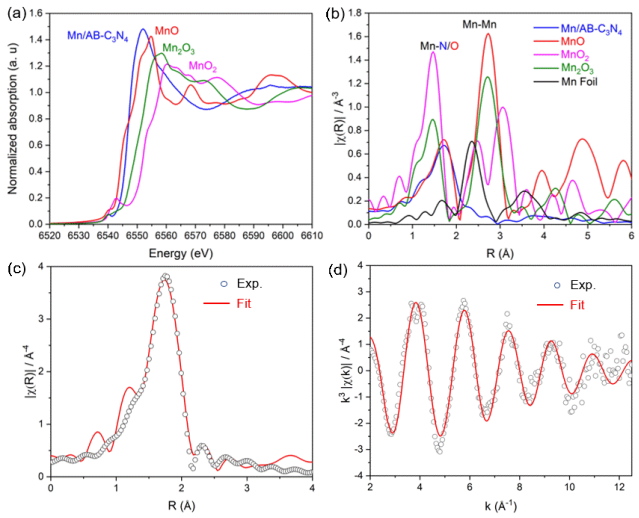

Figure 5. Normalized Mn K-edge XANES spectra (a) and Fourier Transform of the k^3-weighted EXAFS (b) for Mn/AB-C_3N_4 photocatalyst, MnO, Mn_2O_3, MnO_2, and Mn foil. Data (empty circles) and fits (red lines) of the magnitude of FT signal (c) and the k^3-weighted EXAFS signals in k-space (d).

variant (**Figure 6b**), and the positive slope indicated the n-type nature of these semiconductors. The bottom potential of the conduction band (CB) for an n-type semiconductor is generally considered to be approximately 0.2 V more negative than the E_{fb}. So, g-C_3N_4 had the highest CB position at ca. -1.0 V (vs. NHE), followed by Mn/g-C_3N_4 at ca. -0.88 V (vs. NHE), AB-C_3N_4 at ca. -0.70 V (vs. NHE) and Mn/AB-C_3N_4 with ca. -0.70 V (vs. NHE) (**Figure 6b-c**). The valence band maximum (VBM) energy (E_{VB}) of g-C_3N_4 variants were therefore calculated from $E_{CB} + E_g$ and located at ca. 1.68 V (vs. NHE) for g-C_3N_4, followed by Mn/g-C_3N_4 at ca. 1.73 V (vs. NHE), AB-C_3N_4 at ca. 1.86 V (vs. NHE) and Mn/AB-C_3N_4 with ca. 1.90 V (vs. NHE), respectively (**Figure 6c**). These results suggested that all these photocatalysts should participate both in the indirect and direct 2e⁻ oxygen reduction reactions (ORR) to generate H_2O_2 as the reduction potentials of O_2 is less negative than the CB of the photocatalysts as shown in **equations 1, 2, and 5**. On the other hand, the valence band energy (VB) of unmodified g-C_3N_4 is not sufficiently positive to enable $^{\bullet}OH/H_2O$ (2.73 V vs NHE) and $^{\bullet}OH/OH^-$ (1.99 V vs NHE) oxidation reactions. Indeed *h+* in the VB of g-C_3N_4 rarely participated in the direct oxidation of H_2O or OH^- to generate $^{\bullet}OH$[77]. However, the VB of AB-C_3N_4 and Mn/AB-C_3N_4 are more positive and within the potential range of H_2O (direct 2e⁻ WOR to H_2O_2, **equation 6**) and OH^- (the oxidation of OH^- to $^{\bullet}OH$, **equation 7**) oxidation reactions. The PL life-time profiles of all the samples were recorded by time-correlated photon counting (TCSPC) spectroscopy and fitted using a fourth-exponential decay equation (**Figure 6d**). The PL decays of g-C_3N_4, and SA Mn/g-C_3N_4 were measured at an excitation wavelength of 500 nm and those of AB-C_3N_4 and SA Mn/AB-C_3N_4 at 510 nm. The average PL life-times are 11.10 ± 0.12 ns and 5.17 ± 0.07 ns for g-C_3N_4 and SA Mn/g-C_3N_4, respectively, and 13.37 ± 0.30 ns and 4.97 ± 1.00 ns for AB-C_3N_4 and SA Mn/AB-C_3N_4 respectively. After substitution with Mn, the average life-times decreased by more than half, mainly due to a suppression of the long-lifetime recombination, as seen in the fitting parameters in **Table S5**. Also, there is a significant increase in the amplitude of the fast recombination component, suggesting that predominantly very fast radiative recombination could occur after Mn-substitution. These results confirm the more efficient separation of the photogenerated electron-hole pairs promoted by the (incorporated) Mn.

We simulated the electronic and optical properties of the investigated materials and possible reaction mechanisms in working conditions through representative atomistic models that included the experimental observations resorting, first, to RMD and then to QC. We modeled the photocatalyst support as a disordered arrangement of C_3N_4 flakes (either undoped or casually doped with aryl amino groups[66], surrounded by water molecules. Then, we populated it with Mn^{2+} cations in both high (as suggested by Models I-II from **Figure 4f**) and low coordination sites (as indicated by Models III-IV from **Figure 4f**). The most typical configurations sampled during the RMD were extracted, size-reduced, and re-optimized through DFT calculations (HSE06 XC-functional and the 6-31G(d,p) basis set). The computational details of this multi-scale approach are reported in the **SI** (**S5.1-S5.5**).

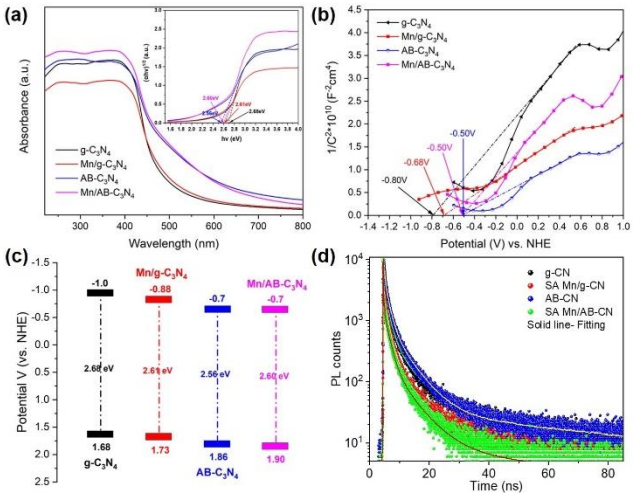

Figure 6. (a) UV–vis absorption spectra and (inset) corresponding UV Vis-DRS Tauc plots of bulk g-C_3N_4 and variants. (b) Mott–Schottky plots of bulk g-C_3N_4 and variants revealing their flat-band potential value collected at 1 kHz frequency versus NHE (Normal Hydrogen Electrode). (c) Electronic band positions of the g-C_3N_4 and variants obtained from the UV-DRS and Mott-Schottky measurements. (d) PL life-time spectra of the powders of g-C_3N_4, SA Mn/g-C_3N_4, AB-C_3N_4, and SA Mn/AB-C_3N_4. The solid line shows the respective fitting of the decay profiles.

The remarkable structural diversity of the derived models strongly influences the local HOMO-LUMO energy difference[78,79], which hardly can be correlated to the

experimental band gap of the material. For example, the two structures depicted in **Figure 7a**, which mimic the Mn/AB-C_3N_4 system and are made of four triazine rings functionalized with an aryl amino ring (whose morphology has been appropriately designed to carry both a high- and a low-coordination site for metal absorption), present a HOMO-LUMO difference of 2.43 eV and 2.99/3.17 eV, respectively (majority and minority bands of the second system have a different HOMO-LUMO gap due to the interaction between magnetic Mn^{2+} and the HOMO state, see DOS in **Figure 7a**). The RMD simulations highlighted the tendency of preserving, around the metal cations, an almost octahedral environment fluctuating in time. This consisted of a combination of N atoms at the edges of the triazine rings (exerting a strong chelating action[7,80,81] and whose number oscillates, in time, between 2 and 4) and water molecules (whose number also oscillates in time between 2 and 4). The two structures of **Figure 7a** represent two distinct families, the former characterized by the Mn^{2+} trapped in a high-coordination site of the g-C_3N_4 matrix, the latter by the Mn^{2+} trapped in a low-coordination site, in close contact with the aryl amino group. In this latter configuration, the distance between Mn^{2+} and one N atom at the edge of the triazine ring is approximately 2.45 Å. This elongated value agrees with the average metal coordination found by EXAFS, which is slightly reduced relative to the ideal value of six. In agreement with the results shown in **Figure 6a**, the simulated excitation of the bare g-C_3N_4 and AB-C_3N_4 systems, see **Figure 7b**, confirmed the decisive role played by the aryl amino group in enhancing visible light absorption in the desired region, in line with literature results about the strong dependence of the optical response of carbon nitride-based systems on structural modification/functionalization[82,83]. The 474 nm HOMO-LUMO strong transition, which dominates the visible part of the simulated spectrum of the AB-C_3N_4 system, is very close to the wavelength of the used LED lamp (427 nm) and clearly shows an electron jump from the aryl amino group (where the HOMO is strongly localized) to the nearest triazine ring (where the LUMO is mainly delocalized[79]). The nature of such an excitation indicates that photo-excited electrons (and corresponding holes) are localized in the neighborhood of the aryl amino group and that the nearby metal cation sites should be considered when simulating the ORR and WOR reaction mechanisms. Further details about the response properties of both g-C_3N_4 and AB-C_3N_4 systems are reported in the **SI** (**S5.2**).

The kinetics of the charge transfer processes of the Mn/AB-C_3N_4 catalysts were studied using electrochemical impedance spectroscopy (EIS). As shown in **Figure S9**, the smaller arc radius of the impedance spectrum indicated smaller charge transfer resistance (R_{CT}) and better electron-hole separation efficiency. Compared to commercial g-C_3N_4, the introduction of aryl amino groups in g-C_3N_4 improves the separation of electron-hole pairs, as indicated by the smaller arc radius. (**Figure S9a**). The Mn/AB-C_3N_4 with the smallest curve radius showed that the atomically dispersed Mn further promoted the separation of e^--h^+ pairs. Additionally, the impedance spectra of the electrodes with Mn/AB-C_3N_4 catalyst were compared in O_2 and N_2 atmosphere under light illumination or in the dark (**Figure S9b**). The Mn/AB-C_3N_4 catalyst in O_2-saturated conditions exhibited a smaller curve size than in N_2-saturated conditions, both under illumination (λ = 427 nm) and in the dark, which indicated that O_2, as an electron acceptor, facilitated the charge separation and prevented the recombination of the photoinduced charges and holes, by consuming the photogenerated electrons at the surface of the photocatalyst. This result was further supplemented by the cyclic voltammetry and the linear sweep voltammetry studies (**Figures S10-S11**). These studies showed that the half-wave potential and onset potential values of Mn/AB-C_3N_4 and AB-C_3N_4 were higher and more positive than the pristine g-C_3N_4, indicating a higher oxygen reduction capability.

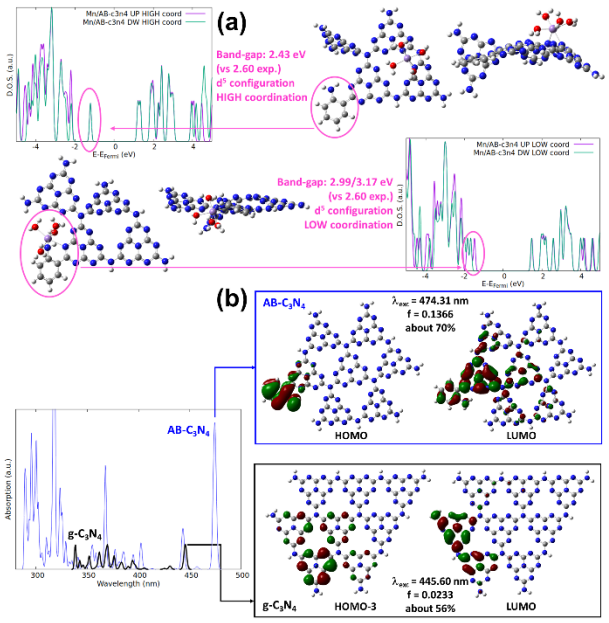

Figure 7. (a) Atomistic structural models and Density Of States (DOS) of two systems optimized at the DFT level, where Mn^{2+} is in a high-coordination site (above) and in a low-coordination site (below); (b) TDDFT spectra of g-C_3N_4 (thick black line) and AB-C_3N_4 (thin blue line) with a specification of the molecular orbitals involved in the main transitions indicated by the arrows.

After the complete structure characterizations and photovoltaic properties investigation of the Mn-AB C_3N_4 catalyst, we performed $^{18}O_2$ labeling and $H_2{}^{18}O$ labeling experiments to identify the oxygen source of the formed H_2O_2. For each labeling experiment, triphenylphosphine (PPh_3) was added to the generated H_2O_2 to provide triphenylphosphine oxide (PPh_3O), which GC-MS analyzed. As shown in **Figure S12a**, when $^{18}O_2$ was used with $H_2{}^{16}O/{}^{16}OH^-$ in the optimized reaction conditions, only $PPh_3{}^{16}O$ was observed. In contrast, when $^{16}O_2$ was used with $H_2{}^{16/18}O/{}^{16/18}OH^-$ (generated in situ by the addition of $K^{16}OH$ to $H_2{}^{18}O$), a mixture of $PPh_3{}^{18}O$ and $PPh_3{}^{16}O$ was observed in **Figure S12b**. Together, the labeling experiments demonstrated that the oxygen source of the formed H_2O_2 was from H_2O/KOH in the liquid phase instead of dioxygen. Therefore, h^+ from Mn/AB-C_3N_4 VB promoted H_2O_2 production in two ways: 1) one-step $2e^-$ WOR process via oxidation of H_2O to H_2O_2; 2) indirect $2e^-$ WOR processes for the generation of $^{\bullet}OH$ from OH^- by h^+, which further combined to generate H_2O_2.

Spin-trapping EPR measurements with 5,5-dimethyl-1-pyrroline N-oxide (DMPO) as a spin-trapping reagent were also performed with illumination from a 447 nm laser source (**Figure S13**) to investigate the reaction mechanism further. In the dark, samples containing AB-C_3N_4 or Mn/AB-C_3N_4 in O_2-saturated aqueous mixtures at pH 7.0, 10.7 or 13.2 (using KOH) with 5,5-dimethyl-1-pyrroline N-oxide (DMPO) only provided some weak signals. Upon illumination, a multi-line spectrum was observed for each sample at pH 7.0 and 10.7, which was simulated using 4 components (R1, R2, R3 and R4 [**Table S6**]). R1 is a 12-line signal and R2 is a 4-line signal with EPR parameters consistent with those of the protonated spin-trapped adduct of $O_2^{\bullet-}$ (DMPO-OOH) and $^{\bullet}OH$ (DMPO-OH), respectively. R3, which had an A_N/A_H ratio of 0.67 was assigned to a DMPO-trapped carbon-centered radical in aqueous media[84], while R4 was a nitroso decay product. In contrast, analogous experiments at pH 13.2 provided only a broad singlet (R5) for AB-C_3N_4 which was assigned to the radical present in g-C_3N_4 (**Table S6**); while for Mn/AB-C_3N_4 a multi-line spectrum was observed which was simulated using R5 and three new components (R6, R7 and R8 [**Table S6**]). The 4-line R6 signal was assigned to the DMPO-O^- adduct, while R7 and R8 were assigned as DMPO-trapped carbon-centered radicals in aqueous media based on their A_N/A_H ratios (0.69 and 0.64, respectively). A significant trend could be found in **Table S7**: in the presence of the Mn sites, the [DMPO-OOH]/[DMPO-O(H)] ratio decreased as pH increased. Assuming the production of $^{\bullet}OH$ from WOR is constant, the trend indicated that the production of $O_2^{\bullet-}$ ($HO_2^{\bullet}$) decreased as pH increased.

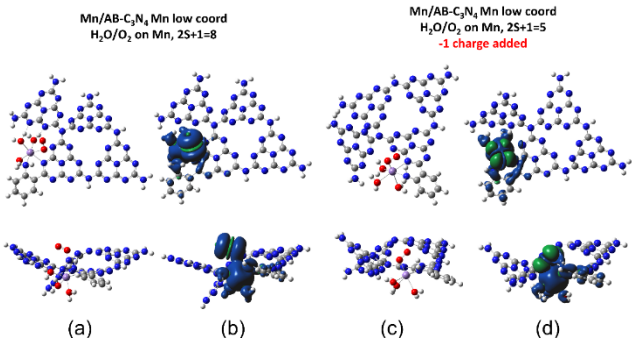

Figure 8. (a) on-top view, side view, and (b) spin-density iso-surface corresponding to O_2 adsorption mode on the Mn^{2+} center in low-coordination site, in contact with an aryl amino group, of the Mn/AB-C_3N_4 system; (c-d) same as (a-b) when an extra-electron is added to the system. Color codes: N blue, C grey, H white, O red, and Mn violet.

Computational chemistry was also used to investigate the possible reaction pathways. In the case of operating conditions, we added O_2 molecules and $(OH)^-$ ions (alkaline medium) to the water solution. The results of RMD confirmed the tendency of protonation/deprotonation of the NH_2 moieties, the hydration of the Mn^{2+} ions by a combination of water and $(OH)^-$ species, their limited motion in the entrapment locations (due to N-chelation), and their ability to attract O_2. Most specifically, we observed a tendency of O_2 to be localized at the edges of the C_3N_4 flakes. Such a phenomenon was examined at the DFT level by considering the interaction between O_2 and the Mn^{2+} located in the low-coordination site according to the models displayed in **Figure 7a**. The resulting configurations are depicted in **Figure 8a-d**, where we can observe that an O_2 species have replaced one water molecule. As shown in **Figure 8a**, without any external perturbation, the interaction of O_2 with Mn^{2+} was relatively weak because of the rather long separation between the nearest oxygen and the metal center, which was 3.4 Å against typical O_{water}-Mn^{2+} and N-Mn^{2+} distances in the 2.1-2.3 Å range. Furthermore, the Mulliken analysis of the charge distribution[85] confirmed the neutrality of the adsorbed O_2, where the O-O separation was approximately 1.2 Å, which is the typical gas phase equilibrium bond distance. In fact, the global spin state of such a structure had a spin multiplicity of 8, resulting from the sum of the d^5 configuration of the photocatalyst and the triplet state of the oxygen molecule, as confirmed by the spin-density iso-surface shown in **Figure 8b**. This picture suggests a limited interaction between the oxygen molecule and the catalyst when no external perturbation is applied and a Mn^{2+} coordination sphere is saturated by water molecules only. Regarding photoexcitation, we reoptimized the structures with an extra electron, finding a quite different scenario. Given the localization of photo-excited electrons in the neighborhood of the aryl amino group (see **Figure 7b**), a mechanism of electron hopping from the substrate to the adsorbed O_2 molecule is strongly supported. The configuration of **Figure 8a** evolved to that of **Figure 8c**, showing an adsorbed O_2 molecule interacting strongly with the metal cation (O-Mn distance reduced to about 2.0 Å), in a local doublet spin-state, with an elongated interatomic O-O length of about 1.3 Å, and negative charge, indicating the formation of superoxide species. Such an effect translated into a lowering of the total spin of the system to 5, with a partial electron coupling between the Mn^{2+} center and the adsorbed O_2 (see spin density iso-surface reported in **Figure 8d**). The deprotonation of the NH_2 moieties upon Mn^{2+} addition observed in NMR was also investigated by the calculations and the discussion is reported in the **SI (S5.3)**.

Moving to the formation of H_2O_2, we primarily focused on the high-coordination site model displayed in **Figure 7b**, which was the nearest site to the photoexcitation process not involved in the interaction with O_2. We noticed that the coordination environment of Mn^{2+} could be populated by a mixture of water molecules and $(OH)^-$, which was reasonably justified by the Coulombic attraction between hydroxyl and metal cations. The local environment of the catalytic site was confirmed by the results of the RMD of a more complex landscape, made of a multilayer C_3N_4 support in a richer water solution containing multiple ions (see **S5.7**). The resulting landscape indicated a possible activation of both the indirect $2e^-$ and the direct $2e^-$ channels of the WOR (**equations 6-9**). Regarding the indirect $2e^-$ path (**equations 7-9**), the starting configuration is shown in **Figure 9a.** After optimizing the related H_2O_2 product (see **Figure 9b**), we investigated both the ground state (absence of photoexcitation) and a modified model where two h^+ were inserted to simulate the photoexcitation. In both cases, the two water molecules were a spectator of the reactive process.

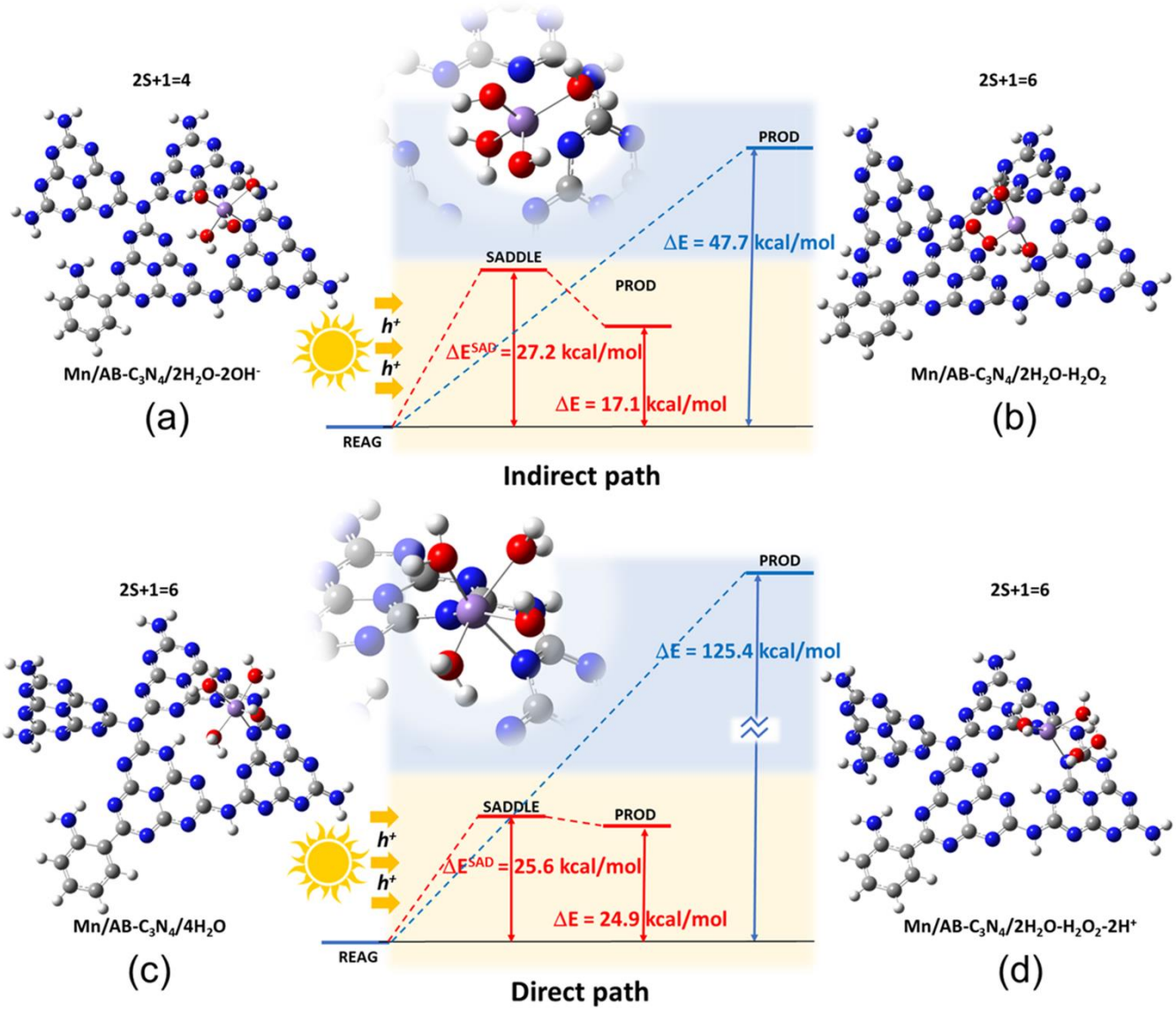

Figure 9. Structures of (a) $2(OH)^-$ + $2H_2O$ (b) $2H_2O$ + H_2O_2; (c) $4H_2O$ and (d) $2H_2O$ + H_2O_2 +$2H^+$ adsorbed on the high-coordinated Mn^{2+} of the Mn/AB-C_3N_4 support. Energy schemes of the both indirect $2e^-$ and direct $2e^-$ paths are shown with a blue background without photoexcitation and with a yellow background when photoexcitation is on. In both cases the structure of the saddle points is displayed within the energy schemes. Color codes: N blue, C grey, H white, O red and Mn violet.

Without photoexcitation, H_2O_2 had a higher energy (47.7 kcal/mol) than the separated OH^-. Thus, the formation of the observed product in these conditions was strongly discouraged. On the contrary, after adding two h^+ to the system, H_2O_2 had a lower energy than in the case above (17.1 kcal/mol higher than the reagents) with an energy barrier (saddle point between separated $(OH)^-$ and H_2O_2) of about 27.2 kcal/mol. The structure of the saddle point (shown in **Figure 9**) is characterized by a reduced distance (by about 0.35 Å) and a smaller angle (by about 17°) between the two $(OH)^-$ oxygens (the final distance in H_2O_2 product is 1.43 Å). The visualized reaction coordinate confirmed that it corresponded to the stretching of the O-O connection. The same mechanism was also simulated for the low-coordination metal site, finding a similar energy scenario (see **SI, S5.4**). This indicates that both environments can activate the indirect channel upon photoexcitation. In the direct $2e^-$ path, among the four water molecules bound to the metal cation (starting configuration in **Figure 9c**), two of them were spectators, whereas one water molecule spontaneously released one hydrogen to the edge of a neighboring triazine ring. In general, the addition of holes facilitates the migration of H atoms to the nitrogen atoms at the edges of the triazine rings. In the direct path one water molecule released a hydrogen to the edges of the triazine rings and the resulting (OH) species reacted to give the expected H_2O_2 product, see **Figure 9d**. Without photoexcitation, products were less stable than reactants by 125.4 kcal/mol: this high energy difference could be symptomatic of the exigence of a charge stabilization of the products. In our model, such stabilization came from the addition of two h^+, which decreased the energy difference between products and reagents to 24.9 kcal/mol (and between saddle point and

reagents to 25.6 kcal/mol) by oxidizing the two hydrogen atoms in the products to protons adsorbed at the electron-rich edges of the triazine rings, as shown in **Figure 9d**. Analogously to the indirect path, also in this case the saddle point is characterized by a reduced distance between the two OH species by about 0.18 Å and a reduced angle by about 22°. Reasonably, the protons resulting from the reaction can be easily removed in alkaline conditions by restoring the catalyst to its native state. All the structured shown in **Figure 8** and **Figure 9** are available as **Supporting Material**.

In agreement with the experimental evidence, these data suggest that the on-set of the photoexcitation process determines the stabilization of the observed product (H_2O_2) *via* the activation of both indirect $2e^-$ and direct $2e^-$ channels of the WOR. The generation of H_2O_2 from Mn/AB-C_3N_4 was unreactive in neutral and acidic environments but had excellent reactivity in an alkaline medium. The proposed mechanisms clearly show that OH^- ions play a crucial role, *direct* in the indirect path as primary actors of the WOR, and *indirect* in the direct path, by neutralizing the products of the WOR (hence promoting the further formation of H_2O_2).

To summarize, we can draw the following overall reaction pathway**.** Under visible light (λ = 427 nm), the Mn/AB-C_3N_4 catalyst quickly absorbs the photon energy to generate the electron-hole pairs, facilitating multiple parallel reactions on its surface. Water oxidation is enabled by the photogenerated holes from the valence band of Mn/AB-C_3N_4, where both direct $2e^-$ WOR and indirect $2e^-$ WOR occurred: (1) photoinduced h^+ directly oxidize H_2O to H_2O_2 *via* the one-step $2e^-$ WOR process (**equation 6**); (2) h^+ first oxidizes hydroxide ion (OH^-) to generate a hydroxyl radical ($^{\bullet}OH$) (**equation 7**), and then produces hydrogen peroxide indirectly by the recombination of two hydroxyl radical (**equation 9**). The existence of an electron accepter of O_2 is to immediately consume electrons to promote the separation of photogenerated electron-hole pairs and to prevent photo corrosion of the photocatalyst. Under working conditions (pH 13), our investigation using EPR spin-trapping revealed no detection of superoxide, and $^{18}O_2$ experiments showed no presence of $H_2{}^{18}O_2$. Additionally, our DFT studies showed that Mn-OOH, a well-known intermediate for $O_2 + 4e^- + 4H^+ \rightarrow 2H_2O$ reaction[86], is present. Therefore, we conclude that $4e^-$ O_2 reduction reaction occurs on the conduction band of this catalyst. The introduction of an aryl amino group shortens the band gap and improves visible light absorption. Furthermore, atomically dispersed Mn atoms on aryl amino-substituted g-C_3N_4 improve the separation efficiency of the photogenerated carriers, inhibit charge recombination, and provide catalytically active sites, which improve the overall photocatalytic efficiency.

CONCLUSIONS

In conclusion, we have developed an Mn-based single-atom catalyst with atomic dispersion of coordinatively unsaturated Mn-Nx sites on aryl amino-substituted graphitic carbon nitride. Comprehensive characterizations confirmed that the Mn species present on the carbon matrix as isolated Mn atoms coordinated with average 4.6 N/O atoms. Notably, this Mn-SAPC exhibited superior catalytic reactivity and stability for the photocatalytic production of H_2O_2 from seawater without the usage of any organic electron donor. Furthermore, the experimental results and theoretical calculations revealed the synergistic function of the unsaturated Mn-Nx sites with a single Mn atom and the adjacent nitrogen atoms at the edges of the triazine rings and aryl amino grafted on g-C_3N_4 skeleton. The introduction of aryl amino groups shortened the band gap and improved light absorption. The Mn-Nx sites facilitated the O_2 adsorption and activation, which accounted for the outstanding catalytic reactivity since they promoted the separation of photogenerated electron-hole pairs and inhibited the recombination of photogenerated electron-hole pairs. In summary, the reported synthetic approach offers an alternative way to synthesize Metal-g-C_3N_4 catalysts with high atomic dispersion and coordinatively unsaturated Metal-Nx sites from nonprecious transition metals, which can be further applied to other (photo)electrocatalytic reactions and organic transformations.

ASSOCIATED CONTENT

Supporting Information
This supporting information is available free of charge via the Internet at:

Additional experimental details, materials, and methods, HR-TEM, XPS analysis, solid-state NMR analysis, XANES and EXAFS analysis, PL spectroscopy, UV-Vis and Mott-Schottky measurements, EIS measurements, ORR measurement, Labeling experiment, EPR study and detailed information of computational chemistry including DFT, molecular dynamics simulations and QC calculations.

AUTHOR INFORMATION

Corresponding Authors

Shoubhik Das - Department of Chemistry, Universiteit Antwerpen, Antwerp 2020, Belgium; **orcid.org/0000-0002-4577-438X; Email:** shoubhik.das@uantwerpen.be

Author

Peng Ren- Department of Chemistry, Universiteit Antwerpen, Antwerp 2020, Belgium; orcid.org/0000-0002-5767-2938
Tong Zhang- Department of Chemistry, Universiteit Antwerpen, Antwerp 2020, Belgium
Noopur Jain- EMAT and NANOlab Center of Excellence, Department of Physics, University of Antwerp, Antwerp 2020, Belgium
H. Y. Vincent Ching- Department of Chemistry, Universiteit Antwerpen, Wilrijk 2610, Belgium
Aleksander Jaworski- Department of Materials and Environmental Chemistry, Stockholm University, Stockholm 10691, Sweden; orcid.org/0000-0002-7156-559X
Giovanni Barcaro- CNR-IPCF, Institute for Chemical and Physical Processes, Area della Ricerca, Pisa I-56124, Italy; orcid.org/0000-0002-5520-5914
Susanna Monti- CNR-ICCOM, Institute of Chemistry of Organometallic Compounds, Area della Ricerca, Pisa I-56124, Italy; orcid.org/0000-0002-3419-7118
Joaquin Silvestre-Albero - Departamento de Química Inorg´anica, Universidad de Alicante, Alicante E-03080, Spain

Veronica Celorrio - Diamond Light Source Ltd, Harwell Science & Innovation Campus, Didcot, Oxfordshire, OX11 0DE, UK
Lata Chouhan - Department of Chemistry, KU Leuven, Leuven 3001, Belgium
Anna Rokicińska - Faculty of Chemistry, Jagiellonian University, Krakow 30-387, Poland; orcid.org/0000-0001-8397-4422
Elke Debroye - Department of Chemistry, KU Leuven, Leuven 3001, Belgium; orcid.org/0000-0003-1087-4759
Piotr Kuśtrowski- Faculty of Chemistry, Jagiellonian University, Krakow 30-387, Poland; orcid.org/00000001-8496-0559
Sabine Van Doorslaer - Department of Chemistry, Universiteit Antwerpen, Wilrijk 2610, Belgium; orcid.org/0000-0002-1685-9202
Sandra Van Aert- EMAT and NANOlab Center of Excellence, Department of Physics, University of Antwerp, Antwerp 2020, Belgium
Sara Bals - EMAT and NANOlab Center of Excellence, Department of Physics, University of Antwerp, Antwerp 2020, Belgium

Author Contributions

The manuscript was written through the contributions of all authors. All authors have given approval to the final version of the manuscript.

Notes

The authors declare no competing interests.

ACKNOWLEDGMENT

S.D. thanks the IOF grant, and Francqui start up grant from the University of Antwerp, Belgium, for the financial support. P.R. thanks CSC, T.Z. thanks FWO for their financial assistance to finish this work. E.D. would like to thank the KU Leuven Research Fund for financial support through STG/21/010. J.S.A. acknowledges financial support from MCIN/AEI/10.13039/501100011033 and EU "NextGeneration/PRTR (Project PCI2020-111968 /3D-Photocat) and Diamond Synchrotron (Rapid access proposal SP32609). We also thank Mr. Jian Zhu, and Mr. Shahid Ullah Khan from the University of Antwerp, Belgium, for helpful discussions.

REFERENCES

(1) Tan, H.; Zhou, P.; Liu, M.; Zhang, Q.; Liu, F.; Guo, H.; Zhou, Y.; Chen, Y.; Zeng, L.; Gu, L.; Zheng, Z.; Tong, M.; Guo, S., Photocatalysis of water into hydrogen peroxide over an atomic Ga-N_5 site. *Nat. Synth.* **2023**, 10.1038/s44160-023-00272-z.
(2) Kaiser, S. K.; Chen, Z.; Faust Akl, D.; Mitchell, S.; Perez-Ramirez, J., Single-Atom Catalysts across the Periodic Table. *Chem. Rev.* **2020,** *120* (21), 11703-11809.
(3) Mitchell, S.; Perez-Ramirez, J., Single atom catalysis: a decade of stunning progress and the promise for a bright future. *Nat. Commun.* **2020,** *11* (1), 4302-4304.
(4) Kaiser, S. K.; Fako, E.; Manzocchi, G.; Krumeich, F.; Hauert, R.; Clark, A. H.; Safonova, O. V.; Lopez, N.; Perez-Ramirez, J., Nanostructuring unlocks high performance of platinum single-atom catalysts for stable vinyl chloride production. *Nat. Catal.* **2020,** *3* (4), 376-385.
(5) Surin, I.; Tang, Z.; Geiger, J.; Damir, S.; Eliasson, H.; Agrachev, M.; Krumeich, F.; Mitchell, S.; Kondratenko, V.A.; Kondratenko, E.V.; Jeschke, G.; Erni, R.; López, N.; Pérez‐Ramírez, J., Low‐Valent Manganese Atoms Stabilized on Ceria for Nitrous Oxide Synthesis. *Adv. Mater.*, **2023**, 2211260-2211274.
(6) Zhao, E.; Li, M.; Xu, B.; Wang, X. L.; Jing, Y.; Ma, D.; Mitchell, S.; Perez-Ramirez, J.; Chen, Z., Transfer Hydrogenation with a Carbon-Nitride-Supported Palladium Single-Atom Photocatalyst and Water as a Proton Source. *Angew. Chem. Int. Ed. Engl.* **2022,** *61* (40), e202207410.
(7) Vile, G.; Albani, D.; Nachtegaal, M.; Chen, Z.; Dontsova, D.; Antonietti, M.; Lopez, N.; Perez-Ramirez, J., A stable single-site palladium catalyst for hydrogenations. *Angew. Chem. Int. Ed. Engl.* **2015,** *54* (38), 11265-9.
(8) Vogt, C.; Weckhuysen, B. M., The concept of active site in heterogeneous catalysis. *Nat. Rev. Chem.* **2022,** *6* (2), 89-111.
(9) Liu, P.; Zhao, Y.; Qin, R.; Mo, S.; Chen, G.; Gu, L.; Chevrier, D. M.; Zhang, P.; Guo, Q.; Zang, D.; Wu, B.; Fu, G.; Zheng, N., Photochemical route for synthesizing atomically dispersed palladium catalysts. *Science* **2016,** *352* (6287), 797-801.
(10) Gu, J.; Hsu, C. S.; Bai, L.; Chen, H. M.; Hu, X., Atomically dispersed Fe^{3+} sites catalyze efficient CO_2 electroreduction to CO. *Science* **2019,** *364* (6445), 1091-1094.
(11) Guo, Y.; Huang, Y.; Zeng, B.; Han, B.; Akri, M.; Shi, M.; Zhao, Y.; Li, Q.; Su, Y.; Li, L.; Jiang, Q.; Cui, Y. T.; Li, L.; Li, R.; Qiao, B.; Zhang, T., Photo-thermo semi-hydrogenation of acetylene on Pd_1/TiO_2 single-atom catalyst. *Nat. Commun.* **2022,** *13* (1), 2648-2659.
(12) Zhang, T.; Sun, Z.; Li, S.; Wang, B.; Liu, Y.; Zhang, R.; Zhao, Z., Regulating electron configuration of single Cu sites via unsaturated N,O-coordination for selective oxidation of benzene. *Nat. Commun.* **2022,** *13* (1), 6996-7003.
(13) Liu, K.; Badamdorj, B.; Yang, F.; Janik, M. J.; Antonietti, M., Accelerated Anti-Markovnikov Alkene Hydrosilylation with Humic-Acid-Supported Electron-Deficient Platinum Single Atoms. *Angew. Chem. Int. Ed. Engl.* **2021,** *60* (45), 24220-24226.
(14) Lee, V.; Park, C.; Jaye, C.; Fischer, D. A.; Yu, Q.; Wu, W.; Liu, Z.; Bao, J.; Pei, S.-S.; Smith, C.; Lysaght, P.; Banerjee, S., Substrate Hybridization and Rippling of Graphene Evidenced by Near-Edge X-ray Absorption Fine Structure Spectroscopy. *J. Phys. Chem. Lett.* **2010,** *1* (8), 1247-1253.
(15) Schultz, B. J.; Patridge, C. J.; Lee, V.; Jaye, C.; Lysaght, P. S.; Smith, C.; Barnett, J.; Fischer, D. A.; Prendergast, D.; Banerjee, S., Imaging local electronic corrugations and doped regions in graphene. *Nat. Commun.* **2011,** *2*, 372-379.
(16) Seifrid, M.; Reddy, G. N. M.; Chmelka, B. F.; Bazan, G. C., Insight into the structures and dynamics of organic semiconductors through solid-state NMR spectroscopy. *Nat. Rev. Mater.* **2020,** *5* (12), 910-930.
(17) Brouwer, D. H.; Cadars, S.; Eckert, J.; Liu, Z.; Terasaki, O.; Chmelka, B. F., A general protocol for determining the structures of molecularly ordered but noncrystalline silicate frameworks. *J. Am. Chem. Soc.* **2013,** *135* (15), 5641-5655.
(18) Seifrid, M. T.; Reddy, G. N. M.; Zhou, C.; Chmelka, B. F.; Bazan, G. C., Direct Observation of the Relationship betweenMolecular Topology and Bulk Morphology for a π-Conjugated Material. *J. Am. Chem. Soc.* **2019,** *141* (13), 5078-5082.
(19) Smith, B. J.; Rawal, A.; Funkhouser, G. P.; Roberts, L. R.; Gupta, V.; Israelachvili, J. N.; Chmelka, B. F., Origins of saccharide-dependent hydration at aluminate, silicate, and aluminosilicate surfaces. *Proc. Natl. Acad. Sci. U. S. A.* **2011,** *108* (22), 8949-8954.
(20) Sun, K.; Shan, H.; Neumann, H.; Lu, G. P.; Beller, M., Efficient iron single-atom catalysts for selective ammoxidation of alcohols to nitriles. *Nat. Commun.* **2022,** *13* (1), 1848-1856.
(21) Papa, V.; Cao, Y.; Spannenberg, A.; Junge, K.; Beller, M., Development of a practical non-noble metal catalyst for hydrogenation of N-heteroarenes. *Nat. Catal.* **2020,** *3* (2), 135-142.
(22) Chang, F.; Guan, Y.; Chang, X.; Guo, J.; Wang, P.; Gao, W.; Wu, G.; Zheng, J.; Li, X.; Chen, P., Alkali and Alkaline Earth Hydrides-Driven N_2 Activation and Transformation over Mn Nitride Catalyst. *J. Am. Chem. Soc.* **2018,** *140* (44), 14799-14806.

(23) Kallmeier, F.; Kempe, R., Manganese Complexes for (De)Hydrogenation Catalysis: A Comparison to Cobalt and Iron Catalysts. *Angew. Chem. Int. Ed. Engl.* **2018,** *57* (1), 46-60.
(24) Gandeepan, P.; Muller, T.; Zell, D.; Cera, G.; Warratz, S.; Ackermann, L., 3d Transition Metals for C-H Activation. *Chem. Rev.* **2019,** *119* (4), 2192-2452.
(25) Campos-Martin, J. M.; Blanco-Brieva, G.; Fierro, J. L., Hydrogen peroxide synthesis: an outlook beyond the anthraquinone process. *Angew. Chem. Int. Ed. Engl.* **2006,** *45* (42), 6962-6984.
(26) Perry, S. C.; Pangotra, D.; Vieira, L.; Csepei, L.-I.; Sieber, V.; Wang, L.; Ponce de León, C.; Walsh, F. C., Electrochemical synthesis of hydrogen peroxide from water and oxygen. *Nat. Rev. Chem.* **2019,** *3* (7), 442-458.
(27) Kato, S.; Jung, J.; Suenobu, T.; Fukuzumi, S., Production of hydrogen peroxide as a sustainable solar fuel from water and dioxygen. *Energy Environ. Sci.* **2013,** *6* (12), 3756–3764.
(28) Yamada, Y.; Yoneda, M.; Fukuzumi, S., High and robust performance of H_2O_2 fuel cells in the presence of scandium ion. *Energy Environ. Sci.* **2015,** *8* (6), 1698-1701.
(29) Wang, J. C.; Cui, C. X.; Kong, Q. Q.; Ren, C. Y.; Li, Z.; Qu, L.; Zhang,Y.; Jiang, K., Mn-Doped g-C_3N_4 nanoribbon for efficient visible-light photocatalytic water splitting coupling with methylene blue degradation. *ACS Sustain. Chem. Eng,* **2018**, *6*(7), 8754-8761.
(30) Zhang, W.; Fernandez-Fueyo, E.; Ni, Y.; van Schie, M.; Gacs, J.; Renirie, R.; Wever, R.; Mutti, F. G.; Rother, D.; Alcalde, M.; Hollmann, F., Selective aerobic oxidation reactions using a combination of photocatalytic water oxidation and enzymatic oxyfunctionalisations. *Nat. Catal.* **2018,** *1* (1), 55-62.
(31) Yan, H.; Shen, M.; Shen, Y.; Wang, X. D.; Lin, W.; Pan, J.; He, J.; Ye, Y. X.; Yang, X.; Zhu, F.; Xu, J.; He, J.; Ouyang, G., Spontaneous exciton dissociation in organic photocatalyst under ambient conditions for highly efficient synthesis of hydrogen peroxide. *Proc. Natl. Acad. Sci. U. S. A.* **2022,** *119* (22), e2202913119.
(32) Hao, Y. C.; Chen, L. W.; Li, J.; Guo, Y.; Su, X.; Shu, M.; Zhang, Q.; Gao, W. Y.; Li, S.; Yu, Z. L.; Gu, L.; Feng, X.; Yin, A. X.; Si, R.; Zhang, Y. W.; Wang, B.; Yan, C. H., Metal-organic framework membranes with single-atomic centers for photocatalytic CO_2 and O_2 reduction. *Nat. Commun.* **2021,** *12* (1), 2682-2692.
(33) Moon, G.-h.; Kim, W.; Bokare, A. D.; Sung, N.-e.; Choi, W., Solar production of H_2O_2 on reduced graphene oxide–TiO_2 hybrid photocatalysts consisting of earth-abundant elements only. *Energy Environ. Sci.* **2014,** *7* (12), 4023-4028.
(34) Ye, Y. X.; Pan, J.; Xie, F.; Gong, L.; Huang, S.; Ke, Z.; Zhu, F.; Xu, J.; Ouyang, G., Highly efficient photosynthesis of hydrogen peroxide in ambient conditions. *Proc. Natl. Acad. Sci. U. S. A.* **2021,** *118* (16), e2103964118.
(35) Krishnaraj, C.; Sekhar Jena, H.; Bourda, L.; Laemont, A.; Pachfule, P.; Roeser, J.; Chandran, C. V.; Borgmans, S.; Rogge, S. M. J.; Leus, K.; Stevens, C. V.; Martens, J. A.; Van Speybroeck, V.; Breynaert, E.; Thomas, A.; Van Der Voort, P., Strongly Reducing (Diarylamino)benzene-Based Covalent Organic Framework for Metal-Free Visible Light Photocatalytic H_2O_2 Generation. *J. Am. Chem. Soc.* **2020,** *142* (47), 20107-20116.
(36) Zhao, W.; Yan, P.; Li, B.; Bahri, M.; Liu, L.; Zhou, X.; Clowes, R.; Browning, N. D.; Wu, Y.; Ward, J. W.; Cooper, A. I., Accelerated Synthesis and Discovery of Covalent Organic Framework Photocatalysts for Hydrogen Peroxide Production. *J. Am. Chem. Soc.* **2022,** *144* (22), 9902-9909.
(37) Shiraishi, Y.; Takii, T.; Hagi, T.; Mori, S.; Kofuji, Y.; Kitagawa, Y.; Tanaka, S.; Ichikawa, S.; Hirai, T., Resorcinol-formaldehyde resins as metal-free semiconductor photocatalysts for solar-to-hydrogen peroxide energy conversion. *Nat. Mater.* **2019,** *18* (9), 985-993.
(38) Shiraishi, Y.; Matsumoto, M.; Ichikawa, S.; Tanaka, S.; Hirai, T., Polythiophene-Doped Resorcinol-Formaldehyde Resin Photocatalysts for Solar-to-Hydrogen Peroxide Energy Conversion. *J. Am. Chem. Soc.* **2021,** *143* (32), 12590-12599.
(39) Teng, Z.; Zhang, Q.; Yang, H.; Kato, K.; Yang, W.; Lu, Y.-R.; Liu, S.; Wang, C.; Yamakata, A.; Su, C.; Liu, B.; Ohno, T., Atomically dispersed antimony on carbon nitride for the artificial photosynthesis of hydrogen peroxide. *Nat. Catal.* **2021,** *4* (5), 374-384.
(40) Chen, Z.; Vorobyeva, E.; Mitchell, S.; Fako, E.; Ortuno, M. A.; Lopez, N.; Collins, S. M.; Midgley, P. A.; Richard, S.; Vile, G.; Perez-Ramirez, J., A heterogeneous single-atom palladium catalyst surpassing homogeneous systems for Suzuki coupling. *Nat. Nanotechnol.* **2018,** *13* (8), 702-707.
(41) Gu, J.; Jian, M.; Huang, L.; Sun, Z.; Li, A.; Pan, Y.; Yang, J.; Wen, W.; Zhou, W.; Lin, Y.; Wang, H. J.; Liu, X.; Wang, L.; Shi, X.; Huang, X.; Cao, L.; Chen, S.; Zheng, X.; Pan, H.; Zhu, J.; Wei, S.; Li, W. X.; Lu, J., Synergizing metal-support interactions and spatial confinement boosts dynamics of atomic nickel for hydrogenations. *Nat. Nanotechnol.* **2021,** *16* (10), 1141-1149.
(42) Cao, S.; Chan, T.-S.; Lu, Y.-R.; Shi, X.; Fu, B.; Wu, Z.; Li, H.; Liu, K.; Alzuabi, S.; Cheng, P.; Liu, M.; Li, T.; Chen, X.; Piao, L., Photocatalytic pure water splitting with high efficiency and value by Pt/porous brookite TiO_2 nanoflutes. *Nano Energy* **2020,** *67*, 104287-104295.
(43) Kou, M.; Wang, Y.; Xu, Y.; Ye, L.; Huang, Y.; Jia, B.; Li, H.; Ren, J.; Deng, Y.; Chen, J.; Zhou, Y.; Lei, K.; Wang, L.; Liu, W.; Huang, H.; Ma, T., Molecularly Engineered Covalent Organic Frameworks for Hydrogen Peroxide Photosynthesis. *Angew. Chem. Int. Ed. Engl.* **2022,** *61* (19), e202200413.
(44) Wei, D.; Tan, Y.; Wang, Y.; Kong, T.; Shen, S.; Mao, S. S., Function-switchable metal/semiconductor junction enables efficient photocatalytic overall water splitting with selective water oxidation products. *Sci. Bull.* **2020,** *65* (16), 1389-1395.
(45) Gopakumar, A.; Ren, P.; Chen, J.; Manzolli Rodrigues, B. V.; Vincent Ching, H. Y.; Jaworski, A.; Doorslaer, S. V.; Rokicinska, A.; Kustrowski, P.; Barcaro, G.; Monti, S.; Slabon, A.; Das, S., Lignin-Supported Heterogeneous Photocatalyst for the Direct Generation of H_2O_2 from Seawater. *J. Am. Chem. Soc.* **2022,** *144* (6), 2603-2613.
(46) Wu, Q.; Cao, J.; Wang, X.; Liu, Y.; Zhao, Y.; Wang, H.; Liu, Y.; Huang, H.; Liao, F.; Shao, M.; Kang, Z., A metal-free photocatalyst for highly efficient hydrogen peroxide photoproduction in real seawater. *Nat. Commun.* **2021,** *12* (1), 483-492.
(47) Mase, K.; Yoneda, M.; Yamada, Y.; Fukuzumi, S., Seawater usable for production and consumption of hydrogen peroxide as a solar fuel. *Nat. Commun.* **2016,** *7*, 11470-11476.
(48) Xue, Y.; Wang, Y.; Pan, Z.; Sayama, K., Electrochemical and Photoelectrochemical Water Oxidation for Hydrogen Peroxide Production. *Angew. Chem. Int. Ed. Engl.* **2021,** *60* (19), 10469-10480.
(49) Fan, W.; Zhang, B.; Wang, X.; Ma, W.; Li, D.; Wang, Z.; Dupuis, M.; Shi, J.; Liao, S.; Li, C., Efficient hydrogen peroxide synthesis by metal-free polyterthiophene via photoelectrocatalytic dioxygen reduction. *Energy Environ. Sci.* **2020,** *13* (1), 238-245.
(50) Zhang, K.; Liu, J.; Wang, L.; Jin, B.; Yang, X.; Zhang, S.; Park, J. H., Near-Complete Suppression of Oxygen Evolution for Photoelectrochemical H_2O Oxidative H_2O_2 Synthesis. *J. Am. Chem. Soc.* **2020,** *142* (19), 8641-8648.
(51) Baek, J. H.; Gill, T. M.; Abroshan, H.; Park, S.; Shi, X.; Nørskov, J.; Jung, H. S.; Siahrostami, S.; Zheng, X., Selective and Efficient Gd-Doped $BiVO_4$ Photoanode for Two-Electron Water Oxidation to H_2O_2. *ACS Energy Lett.* **2019,** *4* (3), 720-728.
(52) Zhao, Q.; Wang, Y.; Lai, W.-H.; Xiao, F.; Lyu, Y.; Liao, C.; Shao, M., Approaching a high-rate and sustainable production of hydrogen peroxide: oxygen reduction on Co–N–C single-atom electrocatalysts in simulated seawater. *Energy Environ. Sci.* **2021,** *14* (10), 5444-5456.
(53) Fukuzumi, S., Production of Liquid Solar Fuels and Their Use in Fuel Cells. *Joule* **2017**, *1* (4), 689-738.
(54) Fukuzumi, S.; Lee, Y. M.; Nam, W., Fuel Production from Seawater and Fuel Cells Using Seawater. *ChemSusChem* **2017**, *10* (22), 4264-4276.
(55) Fukuzumi, S.; Lee, Y. M.; Nam, W., Solar-Driven Production of Hydrogen Peroxide from Water and Dioxygen. *Chem.–Eur. J.* **2018**, *24* (20), 5016-5031.

(56) Wang, W.; Luo, Q.; Li, J.; Li, Y.; Li, L.; Huo, X.; Du, X.; Wang, N., Gold–nickel phosphide heterostructures for efficient photocatalytic hydrogen peroxide production from real seawater. *Inorg. Chem. Front.* **2023**, *10* (6), 1907-1918.
(57) David J. Norris, A. L. E., Steven C. Erwin, Doped Nanocrystals. *Science* **2008,** *319*, 1776-1779.
(58) Wang, J.; Xiong, L.; Bai, Y.; Chen, Z.; Zheng, Q.; Shi, Y.; Zhang, C.; Jiang, G.; Li, Z., Mn-Doped Perovskite Nanocrystals for Photocatalytic CO_2 Reduction: Insight into the Role of the Charge Carriers with Prolonged Lifetime. *Solar RRL* **2022,** *6* (8), 2200294-2200301.
(59) Beaulac, R.; Archer, P. I.; Ochsenbein, S. T.; Gamelin, D. R., Mn^{2+}-Doped CdSe Quantum Dots: New Inorganic Materials for Spin-Electronics and Spin-Photonics. *Adv. Funct. Mater.* **2008,** *18* (24), 3873-3891.
(60) Najafpour, M. M.; Renger, G.; Holynska, M.; Moghaddam, A. N.; Aro, E. M.; Carpentier, R.; Nishihara, H.; Eaton-Rye, J. J.; Shen, J. R.; Allakhverdiev, S. I., Manganese Compounds as Water-Oxidizing Catalysts: From the Natural Water-Oxidizing Complex to Nanosized Manganese Oxide Structures. *Chem. Rev.* **2016,** *116* (5), 2886-2936.
(61) Gao, G.; Jiao, Y.; Waclawik, E. R.; Du, A., Single Atom (Pd/Pt) Supported on Graphitic Carbon Nitride as an Efficient Photocatalyst for Visible-Light Reduction of Carbon Dioxide. *J. Am. Chem. Soc.* **2016,** *138* (19), 6292-6297.
(62) Vilé, G.; Di Liberto, G.; Tosoni, S.; Sivo, A.; Ruta, V.; Nachtegaal, M.; Clark, A. H.; Agnoli, S.; Zou, Y.; Savateev, A.; Antonietti, M.; Pacchioni, G., Azide-Alkyne Click Chemistry over a Heterogeneous Copper-Based Single-Atom Catalyst. *ACS Catal.* **2022,** *12* (5), 2947-2958.
(63) Gupta, S.; Zhao, S.; Wang, X. X.; Hwang, S.; Karakalos, S.; Devaguptapu, S. V.; Mukherjee, S.; Su, D.; Xu, H.; Wu, G., Quaternary FeCoNiMn-Based Nanocarbon Electrocatalysts for Bifunctional Oxygen Reduction and Evolution: Promotional Role of Mn Doping in Stabilizing Carbon. *ACS Catal.* **2017,** *7* (12), 8386-8393.
(64) Huang, Y.; Chen, B.; Duan, J.; Yang, F.; Wang, T.; Wang, Z.; Yang, W.; Hu, C.; Luo, W.; Huang, Y., Graphitic Carbon Nitride (g-C_3N_4): An Interface Enabler for Solid-State Lithium Metal Batteries. *Angew. Chem. Int. Ed.* **2020,** *132* (9), 3728-3733.
(65) Dong, F.; Zhao, Z.; Xiong, T.; Ni, Z.; Zhang, W.; Sun, Y.; Ho, W. K., In situ construction of g-C_3N_4/g-C_3N_4 metal-free heterojunction for enhanced visible-light photocatalysis. *ACS Appl. Mater. Interfaces* **2013,** *5* (21), 11392-11401.
(66) Zhang, T.; Schilling, W.; Khan, S. U.; Ching, H. Y. V.; Lu, C.; Chen, J.; Jaworski, A.; Barcaro, G.; Monti, S.; De Wael, K.; Slabon, A.; Das, S., Atomic-Level Understanding for the Enhanced Generation of Hydrogen Peroxide by the Introduction of an Aryl Amino Group in Polymeric Carbon Nitrides. *ACS Catal.* **2021,** *11* (22), 14087-14101.
(67) Zhang, Y.; Qin, S.; Claes, N.; Schilling, W.; Sahoo, P. K.; Ching, H. Y. V.; Jaworski, A.; Lemière, F.; Slabon, A.; Van Doorslaer, S.; Bals, S.; Das, S., Direct Solar Energy-Mediated Synthesis of Tertiary Benzylic Alcohols Using a Metal-Free Heterogeneous Photocatalyst. *ACS Sustain. Chem. Eng.* **2021,** *10* (1), 530-540.
(68) Keller, K.; Zalibera, M.; Qi, M.; Koch, V.; Wegner, J.; Hintz, H.; Godt, A.; Jeschke, G.; Savitsky, A.; Yulikov, M., EPR characterization of Mn(II) complexes for distance determination with pulsed dipolar spectroscopy. *Phys. Chem. Chem. Phys.* **2016,** *18* (36), 25120-25135.
(69) Un, S., Structure and nature of manganese(II) imidazole complexes in frozen aqueous solutions. *Inorg. Chem.* **2013,** *52* (7), 3803-3813.
(70) Vincent Ching, H. Y.; Demay-Drouhard, P.; Bertrand, H. C.; Policar, C.; Tabares, L. C.; Un, S., Nanometric distance measurements between Mn(II)DOTA centers. *Phys. Chem. Chem. Phys.* **2015,** *17* (36), 23368-23377.
(71) Zhang, J.; Zhang, G.; Chen, X.; Lin, S.; Mohlmann, L.; Dolega, G.; Lipner, G.; Antonietti, M.; Blechert, S.; Wang, X., Co-monomer control of carbon nitride semiconductors to optimize hydrogen evolution with visible light. *Angew. Chem. Int. Ed. Engl.* **2012,** *51* (13), 3183-3187.
(72) Saitow, M.; Neese, F., Accurate spin-densities based on the domain-based local pair-natural orbital coupled-cluster theory. *J. Chem. Phys.* **2018,** *149* (3), 034104.
(73) Jaworski, A.; Hedin, N., Electron correlation and vibrational effects in predictions of paramagnetic NMR shifts. *Phys. Chem. Chem. Phys.* **2022,** *24* (25), 15230-15244.
(74) An, Y.; Wang, S.; Feng, D.; Huang, Y.; Qin, Z.; Li, X.; Wu, Z.; Liu, J., Influence of annealing on the local structure, magnetic and transport properties of Mn-doped SiC films. *J. Phys. D: Appl. Phys.* **2013,** *46* (10), 105004.
(75) Yang, H.; Shang, L.; Zhang, Q.; Shi, R.; Waterhouse, G. I. N.; Gu, L.; Zhang, T., A universal ligand mediated method for large scale synthesis of transition metal single atom catalysts. *Nat. Commun.* **2019,** *10* (1), 4585.
(76) Chen, M.; Li, X.; Yang, F.; Li, B.; Stracensky, T.; Karakalos, S.; Mukerjee, S.; Jia, Q.; Su, D.; Wang, G.; Wu, G.; Xu, H., Atomically Dispersed MnN_4 Catalysts via Environmentally Benign Aqueous Synthesis for Oxygen Reduction: Mechanistic Understanding of Activity and Stability Improvements. *ACS Catal.* **2020,** *10* (18), 10523-10534.
(77) Lin, J.; Tian, W.; Guan, Z.; Zhang, H.; Duan, X.; Wang, H.; Sun, H.; Fang, Y.; Huang, Y.; Wang, S., Functional Carbon Nitride Materials in Photo-Fenton-Like Catalysis for Environmental Remediation. *Adv. Funct. Mater.* **2022,** *32* (24), 2201743-2201773.
(78) Shiraishi, Y.; Kofuji, Y.; Sakamoto, H.; Tanaka, S.; Ichikawa, S.; Hirai, T., Effects of Surface Defects on Photocatalytic H_2O_2 Production by Mesoporous Graphitic Carbon Nitride under Visible Light Irradiation. *ACS Catal.* **2015,** *5* (5), 3058-3066.
(79) Zhai, S.; Guo, P.; Zheng, J.; Zhao, P.; Suo, B.; Wan, Y., Density functional theory study on the stability, electronic structure and absorption spectrum of small size g-C_3N_4 quantum dots. *Comp. Mater. Sci.* **2018,** *148*, 149-156.
(80) Ren, G.; Sun, J.; Zhai, S.; Yang, L.; Yu, T.; Sun, L.; Deng, W., Ambient hydrogenation of carbon dioxide into liquid fuel by a heterogeneous synergetic dual single-atom catalyst. *Cell Reports Physical Science* **2022,** *3* (1), 100705-100719.
(81) Huang, G.; Niu, Q.; Zhang, J.; Huang, H.; Chen, Q.; Bi, J.; Wu, L., Platinum single-atoms anchored covalent triazine framework for efficient photoreduction of CO_2 to CH_4. *Chem. Eng. J.* **2022,** *427*, 131018.
(82) Ho, W.; Zhang, Z.; Xu, M.; Zhang, X.; Wang, X.; Huang, Y., Enhanced visible-light-driven photocatalytic removal of NO: Effect on layer distortion on g-C_3N_4 by H_2 heating. *Appl. Catal. B: Environ.* **2015,** *179*, 106-112.
(83) Chen, Y.; Wang, B.; Lin, S.; Zhang, Y.; Wang, X., Activation of n $\rightarrow$ π^* Transitions in Two-Dimensional Conjugated Polymers for Visible Light Photocatalysis. *J. Phys. Chem. C* **2014,** *118* (51), 29981-29989.
(84) Chignell, A. S. W. L. a. C. F., The NoH value in EPR spin trapping: a new parameter for the identification of 5,5-dimethyl-l-pyrroline-N-oxide spin adducts. *J. Biochem. Bioph. Meth.* **1991,** *22*, 83-87.
(85) Crandell, D. W.; Xu, S.; Smith, J. M.; Baik, M. H., Intramolecular Oxyl Radical Coupling Promotes O-O Bond Formation in a Homogeneous Mononuclear Mn-based Water Oxidation Catalyst: A Computational Mechanistic Investigation. *Inorg. Chem.* **2017,** *56* (8), 4436-4446.
(86) Passard, G.; Dogutan, D. K.; Qiu, M.; Costentin, C.; Nocera, D. G., Oxygen Reduction Reaction Promoted by Manganese Porphyrins. *ACS Catal.* **2018,** *8* (9), 8671-8679.

Table of Contents